(Third Oaxtepec Symposium on Nuclear Physics, Mexico City, Jan. 4-6, 1980)
To be published in Notas de Fisica, Vol. 3 (1980).

CONF-800114--2

# THE INFLUENCE OF NUCLEAR STRUCTURE ON HEAVY-ION FUSION AT SUBBARRIER ENERGIES

R. G. Stokstad
Physics Division
Oak Ridge National Laboratory*
Oak Ridge, TN. 37830 USA

DISCLAIMER

This report was prepared as an account of work sponsored by an agency of the United States Government. Neither the United States Government nor any agency thereof, nor any of their employees, makes any warranty, express or implied, or assumes any legal liability or responsibility for the accuracy, completeness, or usefulness of any information, apparatus, product, or process disclosed, or represents that its use would not infringe privately owned rights. Reference herein to any specific commercial product, process, or service by trade name, trademark, manufacturer, or otherwise, does not necessarily constitute or imply its endorsement, recommendation, or favoring by the United States Government or any agency thereof. The views and opinions of authors expressed herein do not necessarily state or reflect those of the United States Government or any agency thereof.

MASTER

## Abstract

Measurements of the cross section for fusion of projectiles of $^{16}O$ and $^{40}Ar$ with isotopes of Sm have been made at energies below the fusion barrier. The experimental identification of the evaporation residues proceeds through the off-line detection of x-rays from radioactive product nuclei. Large differences are observed in the thresholds for fusion with vibrational and rotational target nuclei.

**********

## I. INTRODUCTION

We are generally interested in the way in which nuclear structure influences the reaction of heavy ions. Nuclear structure is defined somewhat narrowly here as the properties of a nucleus at low excitation energy. In cases where this influence is clear and well understood, we may use reactions to learn about nuclear structure. Coulomb excitation and Coulomb-nuclear interference are two of the few available examples of this procedure. More often, we are studying the reaction mechanism itself and nuclear structure, as we have defined it, may or may not be important. It is important for single and multi-nucleon transfer reactions, and can be used as a tool to

*Research sponsored by the U.S. Department of Energy, Division of Basic Energy Sciences, under Contract No. W-7405-eng-26 with Union Carbide Corporation.

By acceptance of this article, the publisher or recipient acknowledges the U.S. Government's right to retain a nonexclusive, royalty-free license in and to any copyright covering the article.

DISTRIBUTION OF THIS DOCUMENT IS UNLIMITED

investigate such reaction mechanisms as multi-step excitation. There are many examples in which nuclear structure has little effect. Much of what goes on in deep inelastic scattering can be explained without specific recourse to nuclear structure,[1] although there may be some recent evidence to the contrary.[2] Similarly, a number of recent papers examining the systematics of fusion cross sections[3-8] suggest that, once the atomic number and weight of the projectile and target have been specified, the main features of the magnitude and energy dependence of the fusion cross section can be predicted rather well. (Exceptions to this occur in the fusion of very light heavy ions; this is discussed by Jorge Gomez del Campo at this meeting.) The questions arise, to what extent does nuclear structure influence the fusion cross section and where might such effects be most easily observed? If we are successful in finding cases in which nuclear structure is important and can then develop a successful theory for the reaction mechanism, we will have accomplished something significant and intellectually satisfying: it will be a bonus if, eventually, we are able to go further and use this knowledge to learn more about nuclear structure.

We are currently in the first steps of the foregoing scenario for heavy-ion fusion. Nuclear structure effects do emerge, as we shall see, when the bombarding energy is varied across and well below the classical threshold for fusion. They are most easily observed by using a range of targets of the same element whose isotopes undergo a transition from vibrational to rotational excitations. This paper will discuss some recent experiments of this type. The analysis of the results, using simple procedures for calculating fusion cross sections, will serve mainly to demonstrate that we do not yet have a successful theory for the reaction mechanism. However, the outlook appears promising.

## II. EXPERIMENTS

The experiments described in the following were carried out at the Weizmann Institute ($^{16}O$ + Sm) in collaboration with Y. Eisen, S. Kaplanis, D. Pelte, U. Smilansky, and I. Tserruya,[9] and at the Gesellschaft fur Schwerionenforschung ($^{40}Ar$ + Sm) in collaboration with K. D. Hildenbrand, J. V. Kratz, W. Reisdorf, G. Wirth, R. Lucas, and J. Poitou.[10,11]

Since cross sections at energies well below the barrier are very small, the experimental method must be capable of detecting with good precision small quantities of evaporation residues. We decided therefore to make an off-line observation of the x-rays from the radioactive evaporation residues trapped in a catcher foil. A schematic of the experimental apparatus is shown in Fig. 1. The surface barrier detectors monitor the beam during the irradiation so that an absolute normalization may be obtained without having to make an independent measurement of the target thickness. The catcher foils located downstream from the target were made of carbon for $^{16}O$ bombardment or Al (in the case of $^{40}Ar$). The thicknesses were chosen just adequate to stop all the desired residues. In this way radioactive products from reactions with light contaminants in the target, and with the atoms of the catcher foil itself, were not retained. This produced a low background, as shown in Fig. 2. This particular spectrum was obtained in 10 minutes of counting after a one-hour long bombardment. The cross section for fusion of $^{16}O$ + $^{150}Sm$ at 60 MeV (lab) is about 500 microbarns. The smallest cross section measured in this work is $\sim$100 microbarns.

In order to obtain absolute cross sections, it is necessary to know the number of x-rays emitted per disintegration by each of the various isotopes contributing to the measured yield. Such values can be obtained if the decay

scheme has been studied previously and an absolute normalization has been determined. Much work has been done on decay schemes for neutron deficient isotopes in the last decade and evaluated level schemes have been prepared by the Nuclear Data Project at Oak Ridge National Laboratory. From this information it is possible to calculate the number of x-rays originating from electron capture (the shaded areas in Fig. 3) and from the subsequent internal conversion of nuclear transitions (unshaded areas). The individual values shown in Fig. 3 for the decay of isotopes produced by the fusion of $^{16}O$ + Sm are estimated to have an accuracy of $\pm 10\%$. Note that typically 80 $K_\alpha$ x-rays are obtained per 100 decays of an isotope . Since this relatively high yield can be detected with $\sim$5-10% efficiency with a Ge spectrometer, the method is ideal for measuring small cross sections.

Information on the distribution of isotopes produced in the fusion reactions is contained in the time dependence of the delayed x-ray yield. Figures 4 and 5 show a typical case. Parent, daughter and granddaughter activities are observed. The full curves are fits to the data in which the known half-lives and absolute x-ray intensities of each isotope were incorporated. The contributions of the individual isotopes, produced by the evaporation of 2, 3, or 4 neutrons from the $^{166}Yb$ compound nucleus, are indicated in Fig. 5. From analyses such as this the isotopic distributions shown in Fig. 6 have been obtained. They exhibit the behavior expected for evaporation of neutrons from an equilibrated compound nucleus (charged particle emission in these cases is fairly small). Some comparisons with statistical model calculations have been made and show reasonably good agreement.

The cross sections for the production of evaporation residues are shown in Figs. 7 and 8. The error (random plus systematic) on a data point is typically $\pm 10\%$ in Fig. 7 and $\pm 15\%$ in Fig. 8. Since fission competition is

negligible for the Yb residues produced at the relatively low bombarding energies here, the evaporation residue cross sections in Fig. 7 ($^{16}O$ + Sm) are equivalent to the fusion cross section. This is not the case for $^{40}Ar$ + Sm and it was necessary to measure the fusion-fission yield in a separate experiment using a $\Delta E$-E counter telescope. When this contribution is added to the evaporation residue yield, the fusion cross sections shown in Fig. 9 are obtained.

The fusion cross sections shown in Figs. 7 and 9 exhibit variations which become relatively larger as the bombarding energy is lowered. These variations, we shall see, are far in excess of the changes expected for spherical, structureless nuclei whose radii increases simply as $A^{1/3}$.

## III. DISCUSSION

Since the motivation of these experiments is to study the effect of nuclear structure on the fusion of heavy ions, we begin by examining in Fig. 10 some structural aspects of the even-even Sm isotopes. The energy of the first $2^+$ state drops rapidly from its value of 1.65 MeV at the N=82 closed neutron shell of $^{144}Sm$ to a minimum of 82 keV for $^{154}Sm$. Accompanying this rapid change is a strong increase in the quadrupole deformation parameter $\beta_2$ which has been evaluated from the electric quadrupole transition matrix element connecting the ground and first $2^+$ states. The pattern of the higher energy levels ($4^+$,$2^{+1}$,$6^+$, etc.) changes from vibrational to rotational as neutron number increases, with the most rapid change occuring at N=90 where $^{152}Sm$ takes on a recognizably rotational level structure. The parameter $\beta_2$ defined in a rotational model by

$$\beta_2 = [B(E2,0\rightarrow 2)]^{1/2}\ [3ZR_0^2/4\pi]^{-1},$$

where $R_0 = 1.2\ A^{1/3}$ fm, corresponds approximately to an equilibrium deformation for $^{152}Sm$, $^{154}Sm$ and to a root mean square vibrational amplitude for $^{144}Sm$ - $^{150}Sm$. The deviations of the shape of the nuclear surface from sphericity, the motions of the nuclear surface, and the energy and angular momentum which are removed from the relative kinetic energy of target and projectile when these modes become excited — all these factors will influence the fusion cross section above and beyond its dependence on the $A^{1/3}$ variation of the nuclear radius. The problem, then, is how to isolate those factors which are most important in explaining the clear correlation of the fusion cross sections (at subthreshold energies) with the nuclear structure characteristics shown in Fig. 10.

The inclusion of structure effects in the calculation of fusion cross sections presupposes that the fusion of a spherical projectile with a spherical, structureless target can be calculated sufficiently accurately. This, however, cannot be done on an apriori basis. The reason is that at low energies, the barrier penetrability is extremely sensitive to the nuclear radius (more generally, to the height and shape of the barrier) and this cannot be predicted with sufficient accuracy. Thus, one is forced to make a phenomenological determination from fitting experimental data, and, as Fig. 10 shows, a completely structureless target is not available.

The first approximation which we will make in examining the experimental data for $^{16}O$ + Sm is that $^{148}Sm$ is a structureless sphere. Having done this, a real and an imaginary nuclear potential are found which, when inserted into the Schrödinger equation, yield absorption cross sections which reproduce the experimental fusion cross sections for $^{16}O$ + $^{148}Sm$. It is possible to fit the data quite well in this way. The curve drawn to guide the eye

in Fig. 7 is indistinguishable from the fit. Once such an empirical spherical potential is fixed, the effect of a static deformation can be included (again, in an approximate way) by replacing the real and imaginary nuclear radii with

$$R \rightarrow R_p + R_T(\theta)$$

where

$$R_T(\theta) = R_T^0(1 + \sum_{\lambda=2}^{\infty} \beta_\lambda \, Y_\lambda^0(\theta)).$$

Here, $\theta$ specifies the orientation of the axis of symmetry of the deformed nucleus with respect to the direction of the projectile, $Y_\lambda^0$ is the spherical harmonic of order $\lambda$ and $R_T^0$ is the radius of the target in the absence of deformation. The effects of deformation on the Coulomb potential must also be taken into account. The dependence of the combined Coulomb and nuclear potential on $\theta$ is shown in Fig. 11 for $^{16}O + {}^{154}Sm$ and $\beta_2 = 0.27$, $\beta_4 = 0.054$ and $\beta_6 = -0.018$. These deformation parameters were determined from measurements of $\alpha$-particle inelastic scattering.[12] The barrier penetration problem is then solved for each partial wave at every angle $\theta$ yielding

$$\sigma(\theta) = \pi \lambda\!\!\!^{-2} \sum_{\ell=0}^{\infty} (2\ell+1) \, T_\ell(\theta)$$

$$\sigma_{fus} = \int_0^{\pi/2} \sigma(\theta) \sin\theta \, d\theta.$$

The quantities $\sigma(\theta)$ and $\sigma(\theta) \sin\theta$ are shown in Fig. 12. Note that $\sigma(\theta)$ covers four orders of magnitude when the bombarding energy (54.3 MeV, c.m.) is well below the barrier for the spherical case ($\sim$60 MeV). Using this prescription for calculating $\sigma_{fus}$, and setting $\beta_4 = \beta_6 = 0$, $\beta_2$ for the other isotopes of Sm can be determined by fitting the excitation functions for fusion. Again, quite good fits can be obtained this way (such as shown by

the lines to guide the eye in Fig. 7). The resulting values of $\beta_2$ are given by curve a in Fig. 13. As shown here, the deduced values of $\beta_2$ are much smaller than those values obtained by other methods. Lest this failure rest on the assumption that $\beta_2(^{148}Sm) = 0$, the whole process of determining a spherical potential was repeated, this time fitting the $^{148}Sm$ data under the assumption that $\beta_2 = 0.10$ and then again with $\beta_2 = 0.13$. The results are shown in Fig. 13 and indicate that this simple, static approximation for including the effects of static deformation is not sufficiently reliable to be used as tool for nuclear structure measurements. It does show, however, that the effects of deformation are significant, and account for the trends of the experimental data shown in Fig. 7.

It is of interest to ask how large is the discrepancy between the predicted and experimental fusion cross sections when the known values of $\beta_\lambda$ are used. This is shown in Fig. 14 in which the ratio of the cross sections for $^{154}Sm$ and $^{148}Sm$ is plotted. The cross section for $^{154}Sm$ at the lowest energy is predicted to be a factor of three larger than observed experimentally.

Many approximations have been made in arriving at the above classical, static, equivalent-sphere prescription for estimating the effects of deformation. A complete discussion of these approximations and estimates of their consequences is outside the scope of this report and will be presented elsewhere.[13] Suffice it to say that the neglect of dynamic effects seems a likely suspect for the discrepancy with the experimental data. Dynamic effects refer (in classical terms) to 1) the induction of an oblate deformation in the target nucleus by the Coulomb field of the projectile,[14] 2) an induced rotation of the nucleus as the projectile approaches, and 3) the loss of relative kinetic energy associated with each of these. In quantum mechanical language, the coupling of the low-lying vibrational and

rotational levels to the ground state allows a dynamic polarization of the deformed target and the diversion of flux into the excitation of these motions.[15]

We have made some initial estimates of these dynamic effects for the case of 60 MeV $^{16}O$ + $^{154}Sm$. A classical estimate of the rotation before fusion yields $\sim 3.5°$ and an excitation energy of $\sim 128$ keV.[16] The result is a reduction in the $^{154}Sm$ cross section by about a factor of 1.5. (Recall that a reduction factor of $\sim 3$ is needed for agreement.) A quantum mechanical, coupled channels calculation including the $2^+$ and $4^+$ rotational levels yields better agreement, the predicted reduction factor for dynamic effects being $\sim 2$.[17] Dynamic effects on the fusion of $^{16}O$ with $^{148}Sm$, however, have not yet been included. Further studies of this are in progress.[18]

Summarizing the $^{16}O$ + Sm fusion results, static effects appear to dominate the changes seen in the fusion cross section for $^{148}Sm$ and $^{154}Sm$, but the inclusion of dynamic effects will be required to produce agreement between predicted and measured cross sections.

An inspection of Fig. 9 shows that the cross sections for $^{40}Ar$ + Sm at low bombarding energies also depend sensitively on the isotopic number and, hence, nuclear structure of the target. Even though the simple static approximation is not adequate for a precise analysis of the data, it may serve as a useful basis for comparing fusion cross sections induced by different projectiles, in our case, $^{16}O$ and $^{40}Ar$. Such a comparison is of interest because dynamic effects of the type discussed above should become more important and because other degrees of freedom[19] associated with the mass asymmetry of target and projectile might be relevant.

The comparison of the $^{16}O$- and $^{40}Ar$-induced cross sections was done using a different procedure than described above. Instead of integrating the Schrödinger equation for a complex potential, the WKB approximation was used. When, for a given partial wave, the c.m. energy was at or above the barrier height. The Hill-Wheeler expression for the barrier penetrability was used. The real nuclear potential was taken to have an exponential shape as given by a proximity-type model.[10,11,20] Figure 15a shows the results of fitting $^{16}O + {}^{148}Sm$ with essentially all parameters free. The result, curve 3, yields $\beta = 0.18$, which is larger than the experimental value. (There is, of course, an interplay between the parameters describing the spherical potential and the deformation parameter.) Curves 1 and 2 correspond to values of $\beta = 0$ and $\beta = 0.14$. The latter is the experimental value. In Fig. 15b, the results for $^{16}O + {}^{154}Sm$ are shown for values of $\beta = 0.0$, 0.18, 0.27, and 0.33, curves 1-4, respectively. The difference between curve 2 and 3 represents the effect of the different nuclear structures of $^{148}Sm$ and $^{154}Sm$. Note that, here again, the difference in the deduced values of $\beta$ for $^{154}Sm$ and $^{148}Sm$, 0.27 - 0.18 = 0.09, is smaller than the known difference of 0.14 to 0.17.

With the spherical potential thus fixed, and the change in the potential when $^{40}Ar$ is used instead of $^{16}O$ specified by the proximity formulation, the fusion cross sections for $^{40}Ar$ + Sm may be predicted. This is shown in Fig. 16a by curve 1. While the overall agreement appears rather good, the discrepancy at the lowest bombarding is significant; it occurs in the predictions for the other isotopes as well. It appears that the actual barrier for $^{40}Ar$ + Sm is effectively lowered, or easier to penetrate, than would be expected on the basis of an extrapolation of cross sections with $^{16}O$ projectiles. This may reflect the additional degree of freedom mentioned

earlier.[19] In any case it was felt useful to introduce an additional, albeit ad hoc, parameter into the WKB penetrability in order to continue with the comparison of the $^{16}O$ and $^{40}Ar$ data, and to quantitatively compare the fusion of $^{40}Ar$ with the other isotopes of Sm. The WKB penetrability was thus written[10,11]

$$t = \exp\left(-\frac{2}{p}\int_{r_1}^{r_2} \frac{\sqrt{2\mu}}{\hbar}[V - E_{c.m.}]dr\right)$$

where for $p > 1$ the penetrability is increased over the usual WKB value (Note that taking $p > 1$ is equivalent to using a smaller reduced mass, $\mu$.) Curve 2 in Fig. 16a shows an excitation function for $\beta = 0.27$ and $p = 1.6$. Allowing both $\beta$ and p to be free parameters yields curve 2 in Fig. 16b; the best fit value of $\beta$ is now 0.24. The sensitivity of the predicted excitation function to the value of $\beta$ when p is held fixed is illustrated in Fig. 16c.

The fits to the data for $^{148}Sm$ and $^{144}Sm$ are shown in Figs. 17 and 18, respectively. With the value of p fixed at 2.1, best-fit values of $\beta$ are 0 and 0.14 for $^{144}Sm$ and $^{148}Sm$, respectively. A new feature emerges with these results, however. This feature may be noted already in the data shown in Fig. 9 — the fusion cross sections for $^{148}Sm$ no longer approach (as rapidly) those of $^{154}Sm$ as the bombarding energy is raised above the barrier. See Fig. 7 for comparison. Such an effect is not contained in any static model for the fusion cross section and this is reflected in the poor agreement at high energies shown in Figs. 17 and 18. An explanation for this currently is not available. However, it seems reasonable to suspect that this difference is connected with the fact that $^{144,148}Sm$ are vibrational whereas $^{154}Sm$ is rotational. This effect first appears with a heavy projectile suggests that it is dynamic in nature because of the much stronger excitation

of collective levels by $^{40}Ar$ than by $^{16}O$. The dynamic effects which were mentioned previously (and shown to decrease the fusion cross section at low energies) are not in evidence in this comparison of $^{16}O$ and $^{40}Ar$. Whereas they should have caused a decrease in the experimental cross section relative to the prediction shown in Fig. 16a by curve 1, the opposite was found to occur. These particular dynamic effects appear to be overshadowed by the possible effect of the additional degree of freedom apparently associated with the size of the projectile.

## IV. SUMMARY AND OUTLOOK

Measurements of fusion cross sections at subbarrier energies have been done by observing the x-rays from radioactive products which are the residues of compound nucleus decay. This method has enabled the determination of cross sections at the level of 100 μb with an absolute accuracy of ±15% or less. The fusion cross sections for $^{16}O$ + Sm and $^{40}Ar$ + Sm exhibit a behavior at low energies which is clearly correlated with the changes in the nuclear structure of the Sm isotopes. The effects are relatively larger, the lower the bombarding energy. A detailed static analysis of these cross sections in terms of nuclear deformation shows that the equilibrium deformation of $^{154}Sm$ is an important aspect influencing the cross section for fusion at low energies. However, such an explanation is insufficient to provide qualitative agreement with the data: significant discrepancies with experiment still remain. Dynamic effects seem a promising avenue for exploration as some initial estimates have yielded encouraging results. The nature of fusion process seems affected by the size of the projectile in ways not consistent with the expected changes in nuclear potential and reduced mass of the system. These inconsistencies appear at both low and high energies

in the $^{40}Ar$ + Sm data. One way of interpreting the observations for $^{40}Ar$ + Sm at low energies is in terms of an additional degree of freedom in the specification of the nuclear potential for $^{40}Ar$ + Sm (e.g. an elongation or necking-in coordinate).

This area of study is ripe for theoretical input. There are a number of ways of treating the dynamics of the problem (classical, semi-classical,[21] quantum-mechanical) and ways of incorporating the nuclear structure information (static deformation, coupled channels, zero point motion of the ground state[22].) Equally important, there are reasonably precise experimental data now available to test these theories. New theoretical methods for understanding these phenomena would provide important motivation and guidance for future experiments.

References

1. W. U. Schröder and J. R. Huizenga, Ann. Rev. Nucl. Sci. 27, 465 (1977).
2. U. Lynen, Proc. Symposium on Nuclear Physics in Heavy-Ion Collisions between 10 and 300 MeV/nucleon, Brookhaven, July 1979.
3. L. C. Vaz and J. M. Alexander, Phys. Rev. C10, 464 (1974).
4. R. Bass, Phys. Rev. Letts. 39, 265 (1977).
5. L. C. Vaz and J. M. Alexander, Phys. Rev. C18, 2152 (1978).
6. J. R. Birkelund, J. R. Huizenga, J.N. De, and D. Sperber, Phys. Rev. Letts. 40, 1123 (1978).
7. H. J. Krappe, J. R. Nix, and A. J. Sierk, Phys. Rev. Letts. 42, 215 (1979).
8. J. R. Birkelund, L. E. Tubbs, J. R. Huizenga, J. N. De, and D. Sperber, Physics Report, to be published.
9. R. G. Stokstad, Y. Eisen, S. Kaplanis, D. Pelte, U. Smilansky, and I. Tserruya, Phys. Rev. Letts. 41, 465 (1978); sumbitted to Phys. Rev. C.
10. W. Reisdorf, Proc. VIIth Int. Workshop on Gross Properties of Nuclei and Nuclear Excitations, Hirschegg, Austria, Jan. 22-27, 1979; Proc. XIIth Int. Summer School in Nuclear Physics, Mikolajki, Poland 1979.
11. R. G. Stokstad, K. D. Hildenbrand, J. V. Kratz, W. Reisdorf, G. Wirth, R. Lucas, and J. Poitou, to be submitted to Z. Physik.
12. D. L. Hendrie, N. K. Glendenning, B. G. Harvey, O. N. Jarvis, H. H. Duhm, J. Sandinos, and J. Mahoney, Phys. Letts. 26B, 127 (1968).
13. R. G. Stokstad and E. E. Gross, to be published (1980).
14. P. W. Riesenfeldt and T. D. Thomas, Phys. Rev. C2, 711 (1970).
15. H. Freiesleben and J. R. Huizenga, Nucl. Phys. A224, 503 (1974).
16. S. Levit, private communication (1978).
17. A. J. Baltz, private communication (1978).
18. E. E. Gross, private communication (1979).

References (cont'd)

19. T. Kodama, R.A.M.S. Nazareth, P. Moller, and J. R. Nix, Phys. Rev. C17, 111 (1978).

20. J. Blocki, J. Randrup, W. J. Swiatecki, and C. F. Tsang, Ann. Phys. (NY) 105, 427 (1977).

21. K. Möhring and U. Smilansky, preprint (1979).

22. H. Esbensen, A. Winther, R. A. Broglia, and C. H. Dasso, Phys. Rev. Letts. 41, 296 (1978); private communication (1979).

## FIGURE CAPTIONS

Fig. 1. Schematic diagram of the apparatus used for producing evaporation residues and trapping them in catcher foils. The latter are indicated by the diagonal lines next to the water-cooled surface.

Fig. 2. Photon spectrum covering the range from 45-53 keV. The Tm $K_{\alpha 1}$ and $K_{\alpha 2}$ x-rays are produced by the electron capture decay of Yb and subsequent internal conversion in the Tm daughter. The full curve is a fit to the data in which each component is approximated by a Gaussian.

Fig. 3. Absolute x-ray intensities from the decay of various isotopes produced in the fusion of $^{16}O$ + Sm.

Fig. 4. The x-ray count rate as a function of time. The length of the bombardment was 28 minutes. The full curves are fits to the data incorporating known half-lives and absolute x-ray intensities.

Fig. 5. The time dependence of the parent activity and the deduced contributions of the 2n, 3n and 4n activities. Note that measurements at later times effectively determine the 2n portion.

Fig. 6. The distribution of the evaporation residues as a function of bombarding energy for the four systems studied. The value of n denotes the number of mass units evaporated by the compound nucleus. The yields are expressed as a percentage of the total fusion cross section. The lines are only to guide the eye.

Fig. 7. The fusion cross sections as a function of bombarding energy.[9] The fusion cross sections, similar at energies well above the fusion barrier, vary markedly at low energies with the more deformed isotopes having the larger cross sections. The lines are to guide the eye.

Fig. 8. The measured evaporation residue cross sections for the fusion of $^{40}Ar + ^{144,148,154}Sm$.[10,11]

Fig. 9. The measured value of the fusion cross section which is the sum of the cross sections for evaporation residue production and for fusion-fission. A data point is shown at each energy for which <u>either</u> an evaporation residue <u>or</u> a fusion-fission measurement was made. The unmeasured quantity at that energy was obtained by interpolation.[10,11]

Fig. 10. The energies of the first excited states of the even-even Sm nuclei and the parameter $\beta$ describing the quadrupole collectivity.

Fig. 11. Barrier heights for the fusion of $^{16}O + ^{154}Sm$. The parameters describing the $\lambda = 2$, 4 and 6 deformations of $^{154}Sm$ were taken from ref. 12.

Fig. 12. Fusion cross sections calculated as a function of the orientation of the deformed nucleus with respect to the direction of the projectile. The dashed line includes of the target before fusion.

Fig. 13. Values of $\beta_2$ deduced from various types of measurements. The values deduced from fusion depend on the value of $\beta_2$ assumed for $^{148}Sm$.

Fig. 14. Ratios of the fusion cross sections for $^{154}Sm$ and $^{148}Sm$. Curve c shows the effects of the lab-cm difference in energy (only), curve b the effects of an $A^{1/3}$ change in the radius (only) and curve a, these effects combined. Spherical nuclei are assumed. Curve d is the static calculation for the indicated deformation parameters. Curve e includes the effects of requiring the deformed nucleus to have the same volume as its spherical equivalent.

Fig. 15. a) Experimental values of $\sigma_{fus}$ for $^{16}O + {}^{148}Sm$. The fits to the data are calculated using a real potential only and the WKB method.

b) Same as a) but for $^{16}O + {}^{154}Sm$.

Fig. 16. Experimental values of $\sigma_{fus}$ for $^{40}Ar + {}^{154}Sm$

a) Curve 1 is calculated using the ordinary WKB penetrability and parameters fixed by fitting $^{16}O + {}^{154}Sm$ (i.e. $\beta_2 = 0.27$). Curve 2 has the parameter p = 1.6 (see text) and all other values the same.

b) Curve 2 is the best fit when both p and $\beta$ are adjusted.

c) Shows the sensitivity of the predicted cross section to changes in $\beta_2$ when p is fixed.

Fig. 17. Experimental values of $\sigma_{fus}$ for $^{40}Ar + ^{148}Sm$. Both curves have the penetrability factor p = 2.1; curve 1 has $\beta_2 = 0$, curve 2 has $\beta_2 = 0.14$.

Fig. 18. Experimental values of $\sigma_{fus}$ for $^{40}Ar + ^{144}Sm$. Curve 1 has the penetrability factor p = 1.0, while it is 2.1 for curves 2 and 3.

ORNL-DWG 79-10674

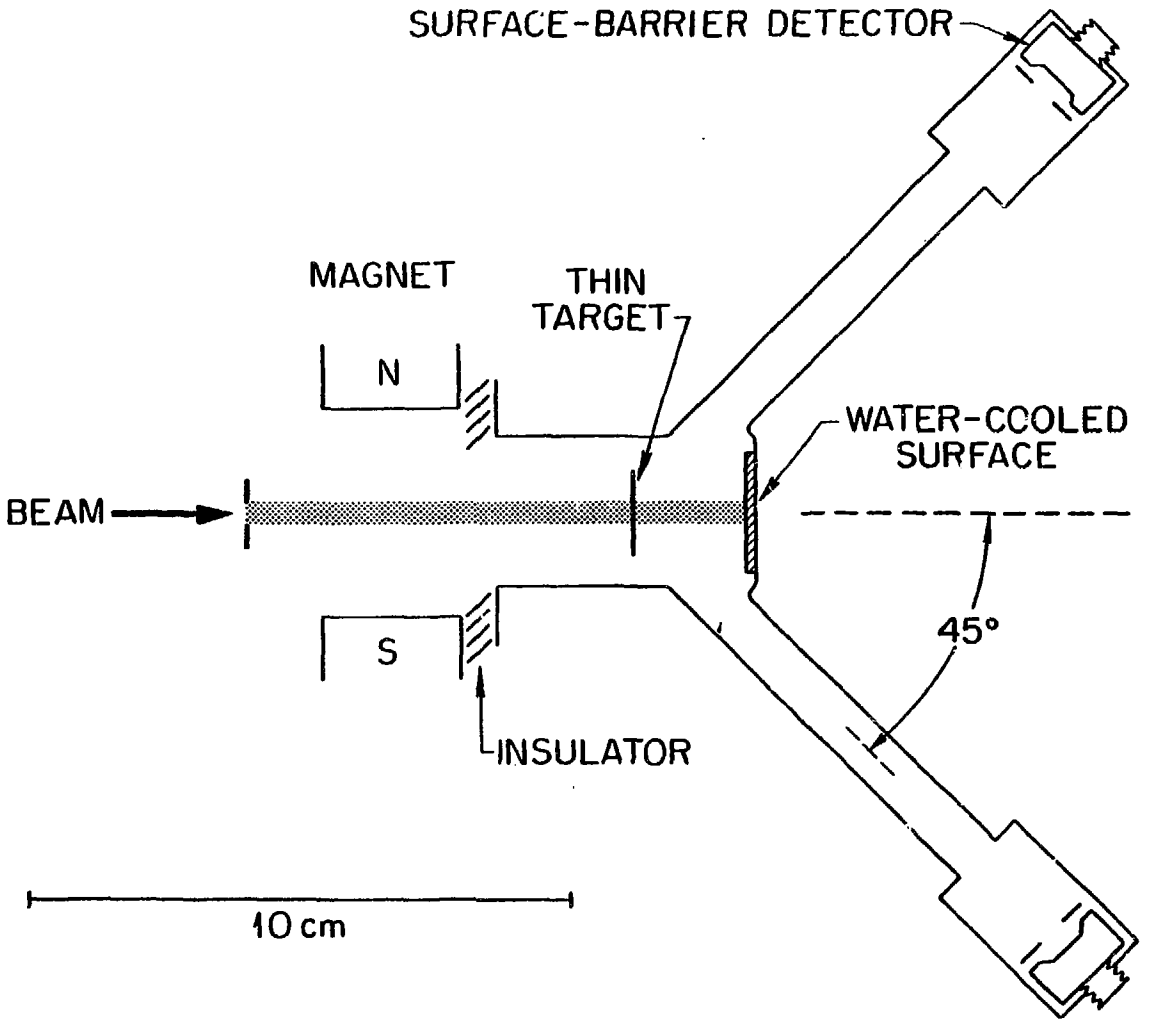


FIG. 1

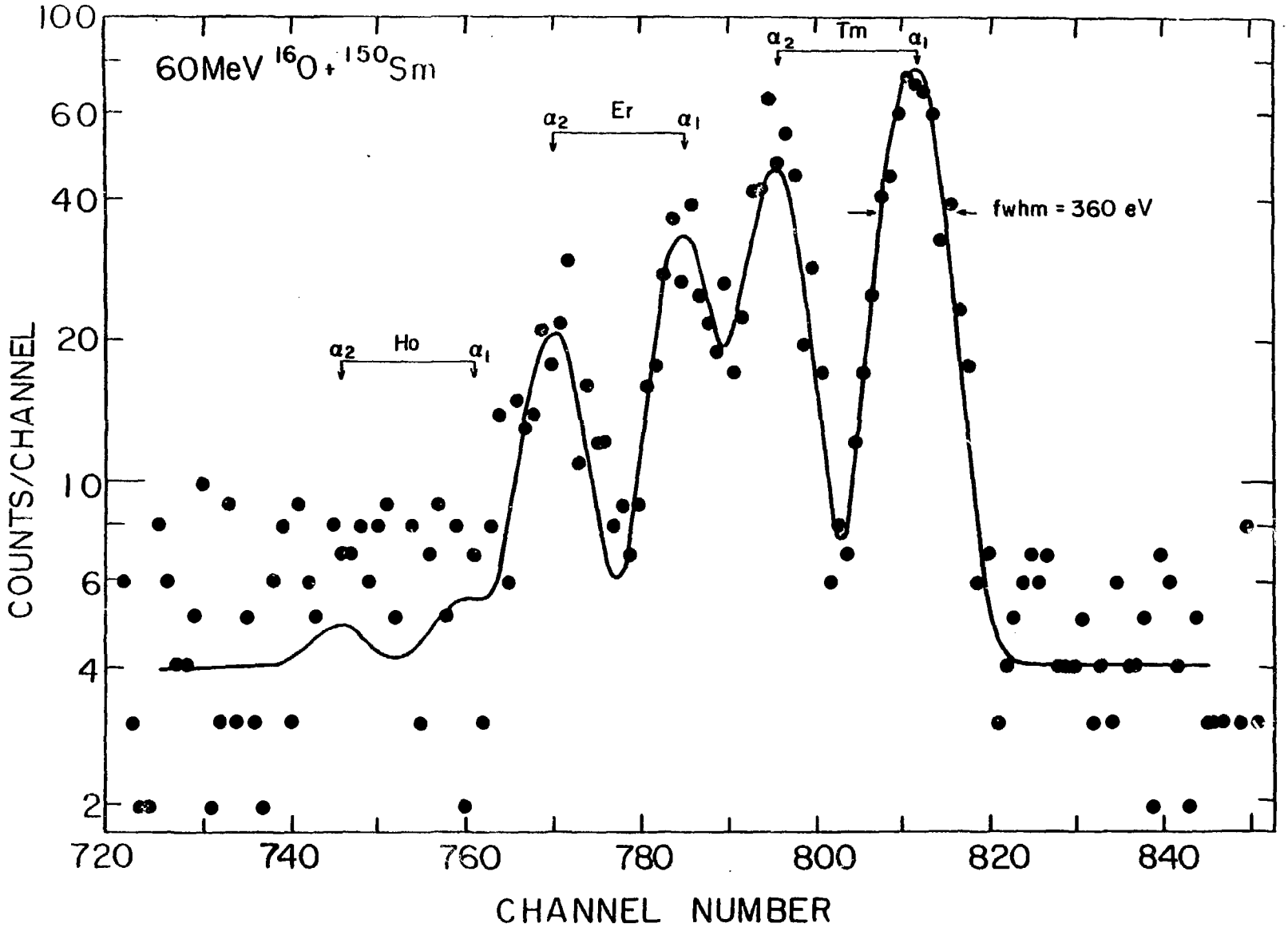
60MeV $^{16}O + ^{150}Sm$
Ho
Er
Tm
$\alpha_2$
$\alpha_1$
fwhm = 360 eV
COUNTS/CHANNEL
CHANNEL NUMBER
100
60
40
20
10
6
4
2
720
740
760
780
800
820
840

FIG. 2

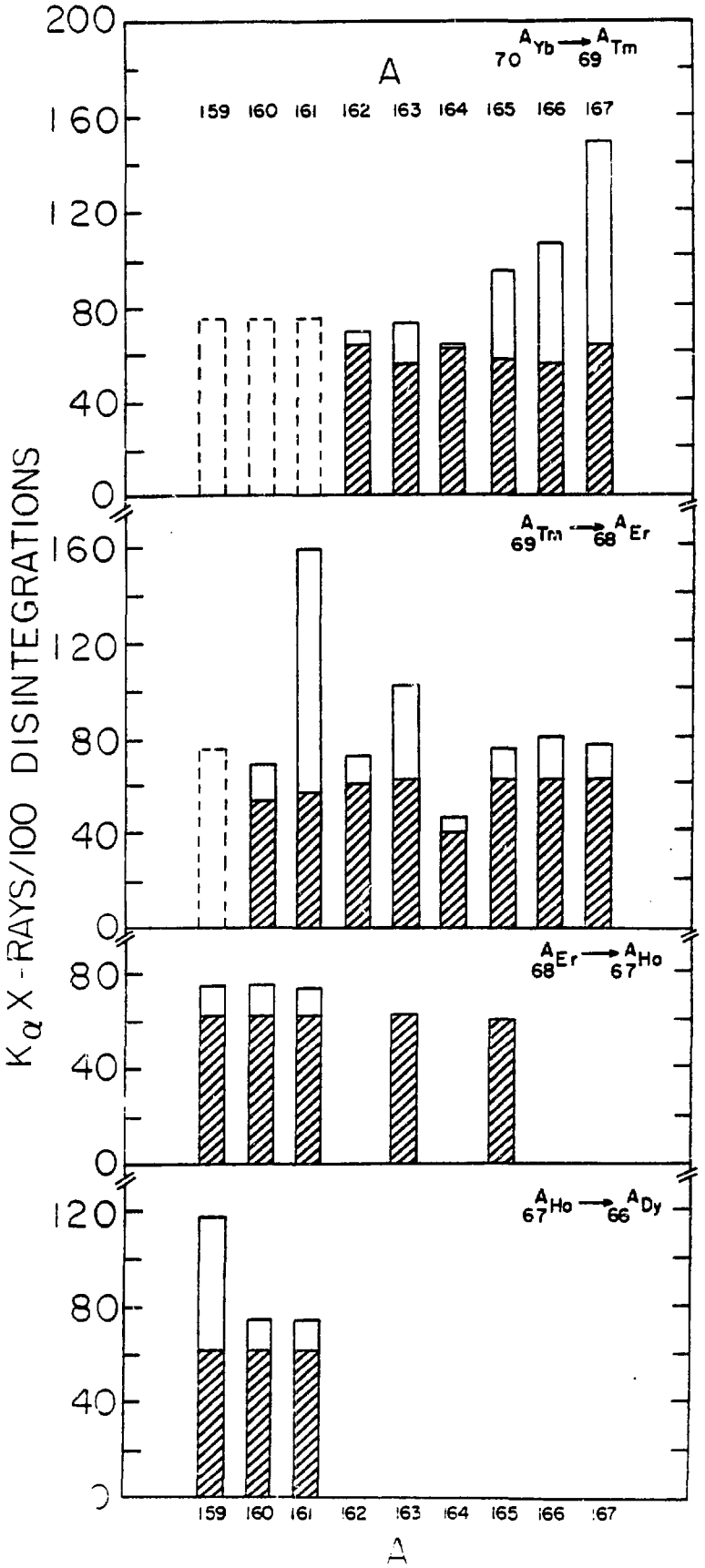
$K_\alpha$ X-RAYS/100 DISINTEGRATIONS
A
$^{A}_{70}Yb \rightarrow ^{A}_{69}Tm$
$^{A}_{69}Tm \rightarrow ^{A}_{68}Er$
$^{A}_{68}Er \rightarrow ^{A}_{67}Ho$
$^{A}_{67}Ho \rightarrow ^{A}_{66}Dy$
159 160 161 162 163 164 165 166 167
A

FIG. 3

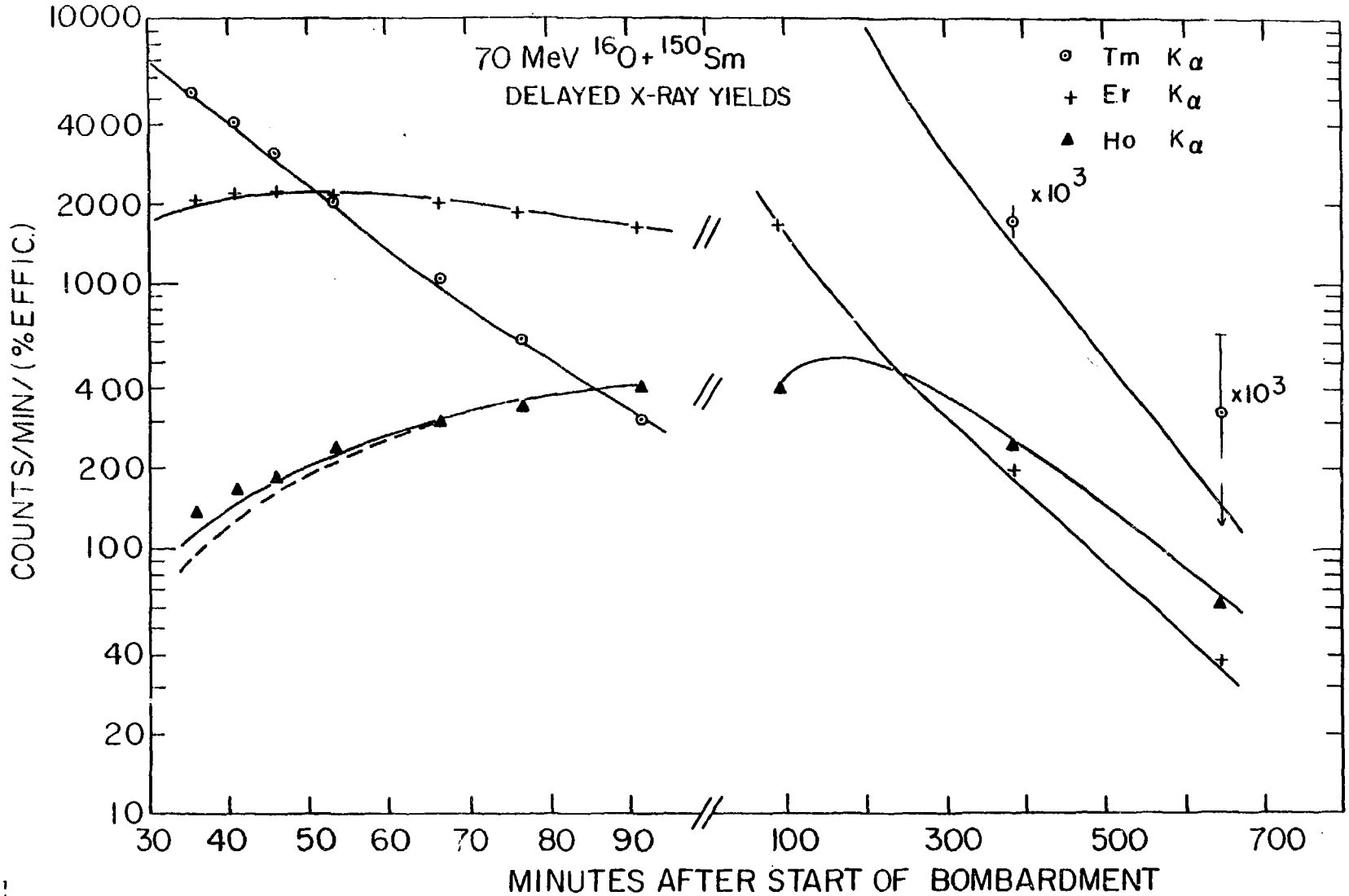
70 MeV $^{16}O + ^{150}Sm$
DELAYED X-RAY YIELDS
Tm $K_\alpha$
Er $K_\alpha$
Ho $K_\alpha$
x10$^3$
x10$^3$
COUNTS/MIN/(%EFFIC.)
10000
4000
2000
1000
400
200
100
40
20
10
30
40
50
60
70
80
90
100
300
500
700
MINUTES AFTER START OF BOMBARDMENT

FIG. 4

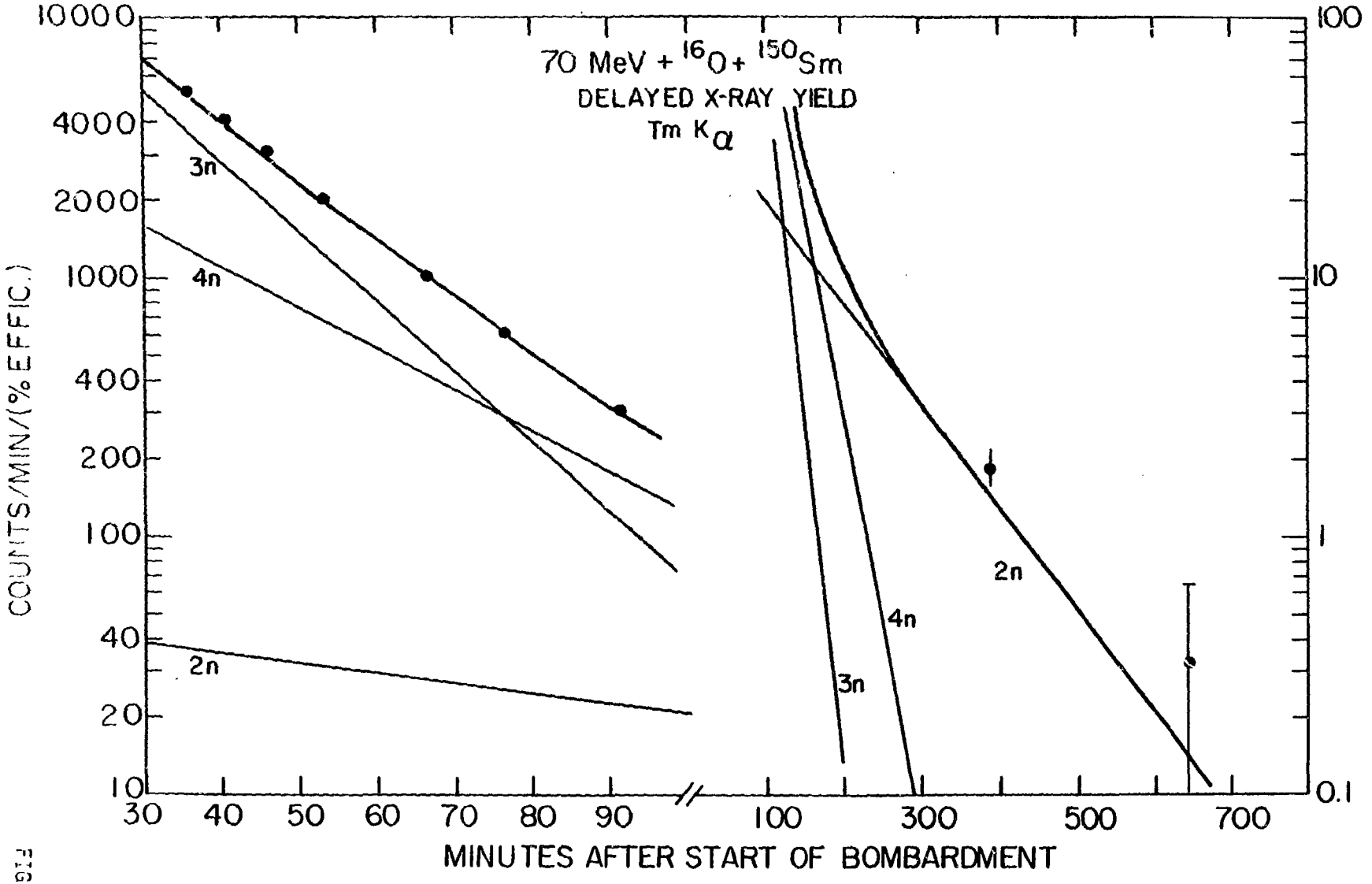
70 MeV + $^{16}O$ + $^{150}Sm$
DELAYED X-RAY YIELD
Tm $K_\alpha$
COUNTS/MIN/(% EFFIC.)
MINUTES AFTER START OF BOMBARDMENT
3n
4n
2n
3n
4n
2n
10000
4000
2000
1000
400
200
100
40
20
10
100
10
1
0.1
30
40
50
60
70
80
90
100
300
500
700

FIG. 5

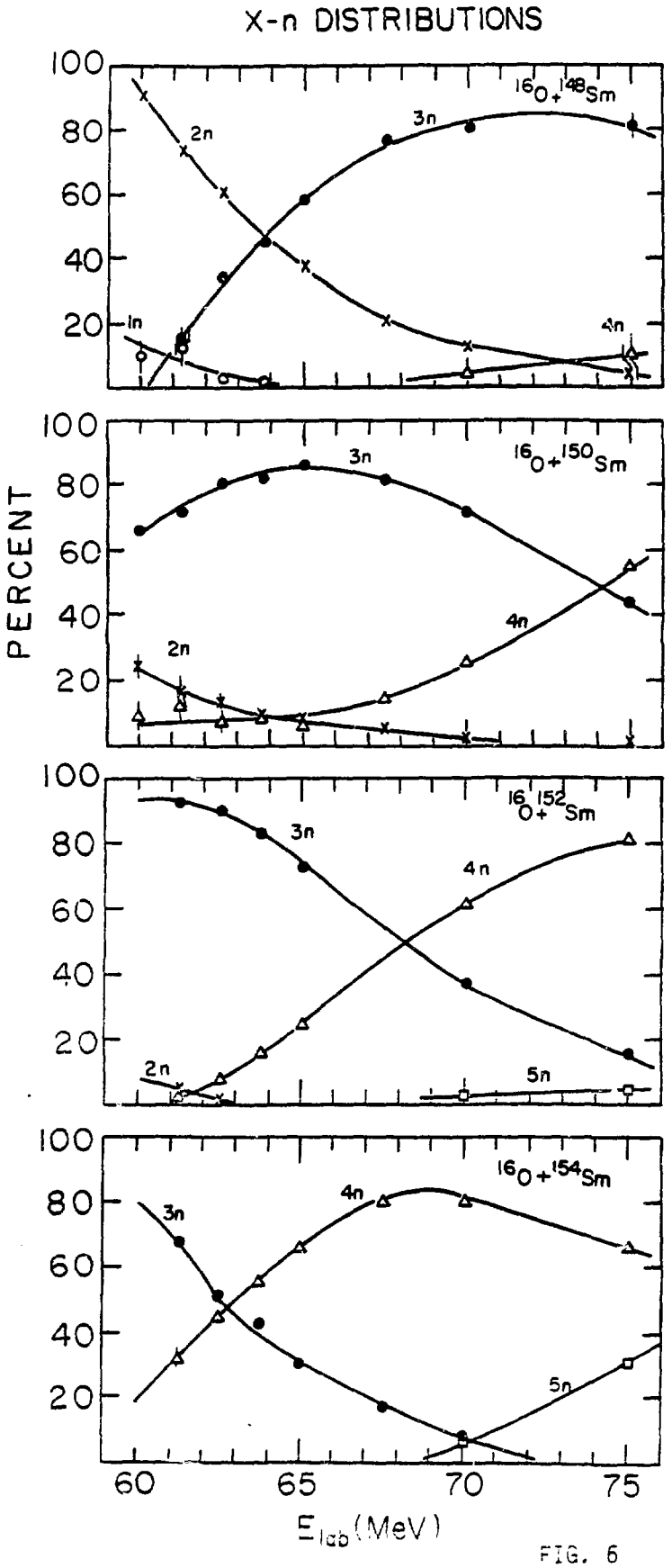
X-n DISTRIBUTIONS
$^{16}O+^{148}Sm$
$^{16}O+^{150}Sm$
$^{16}O+^{152}Sm$
$^{16}O+^{154}Sm$
1n
2n
3n
4n
5n
PERCENT
100
80
60
40
20
60
65
70
75
$E_{lab}$(MeV)

FIG. 6

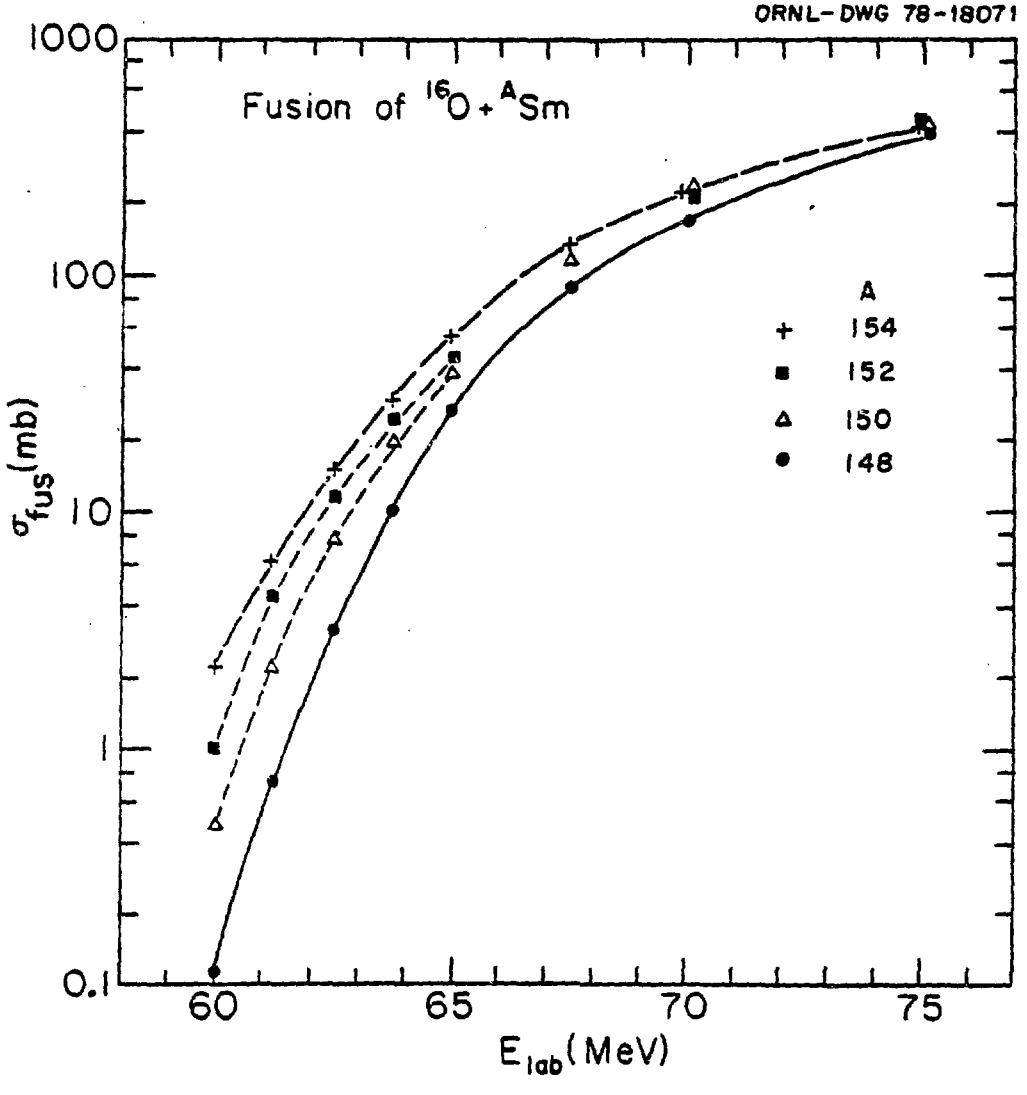
ORNL-DWG 78-18071
Fusion of $^{16}O + ^{A}Sm$
A
154
152
150
148
$\sigma_{fus}$(mb)
1000
100
10
1
0.1
60
65
70
75
$E_{lab}$(MeV)

FIG. 7

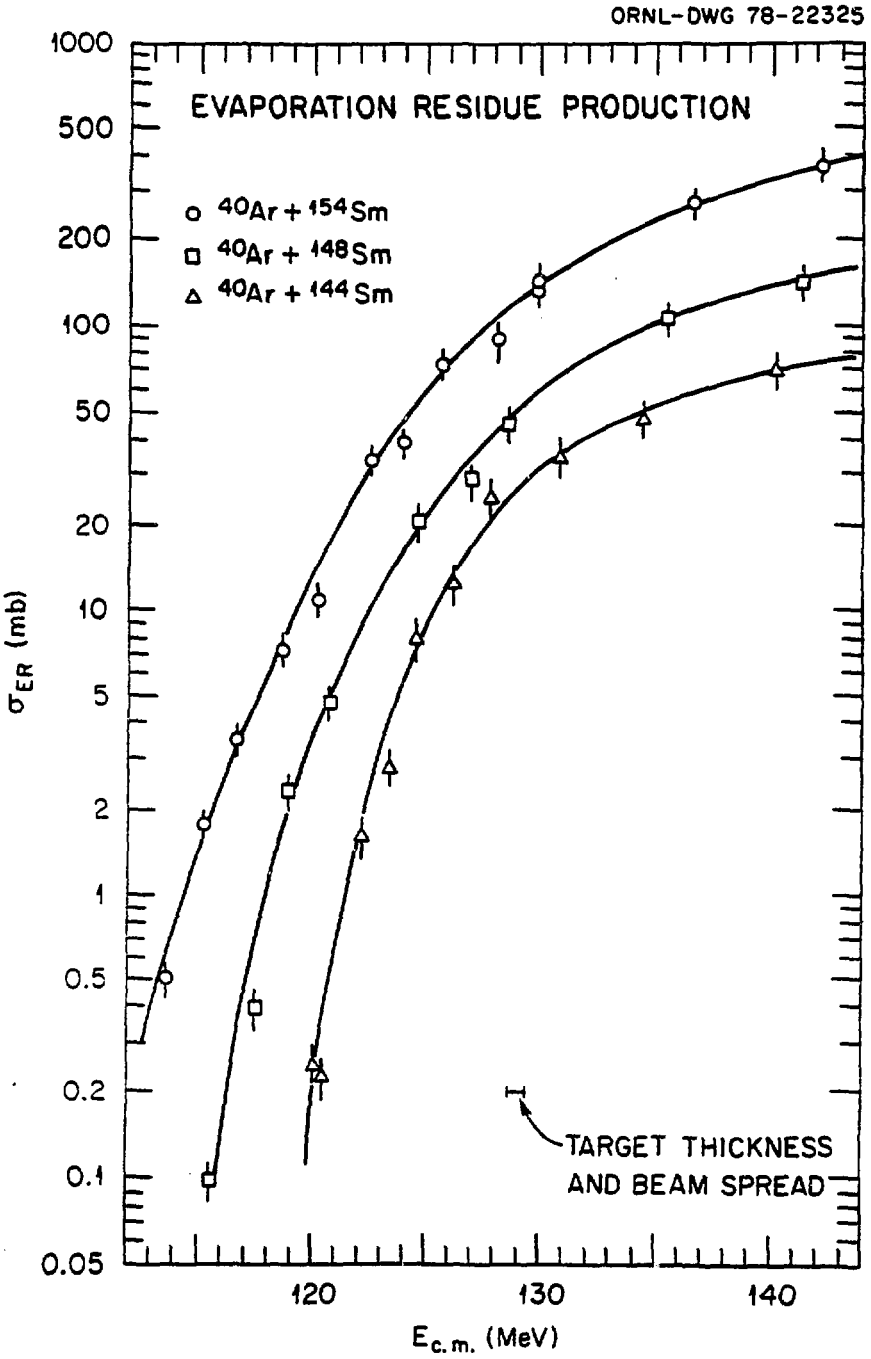
ORNL-DWG 78-22325
EVAPORATION RESIDUE PRODUCTION
o 40Ar + 154Sm
□ 40Ar + 148Sm
△ 40Ar + 144Sm
TARGET THICKNESS
AND BEAM SPREAD
σER (mb)
1000
500
200
100
50
20
10
5
2
1
0.5
0.2
0.1
0.05
120
130
140
Ec.m. (MeV)

FIG. 8

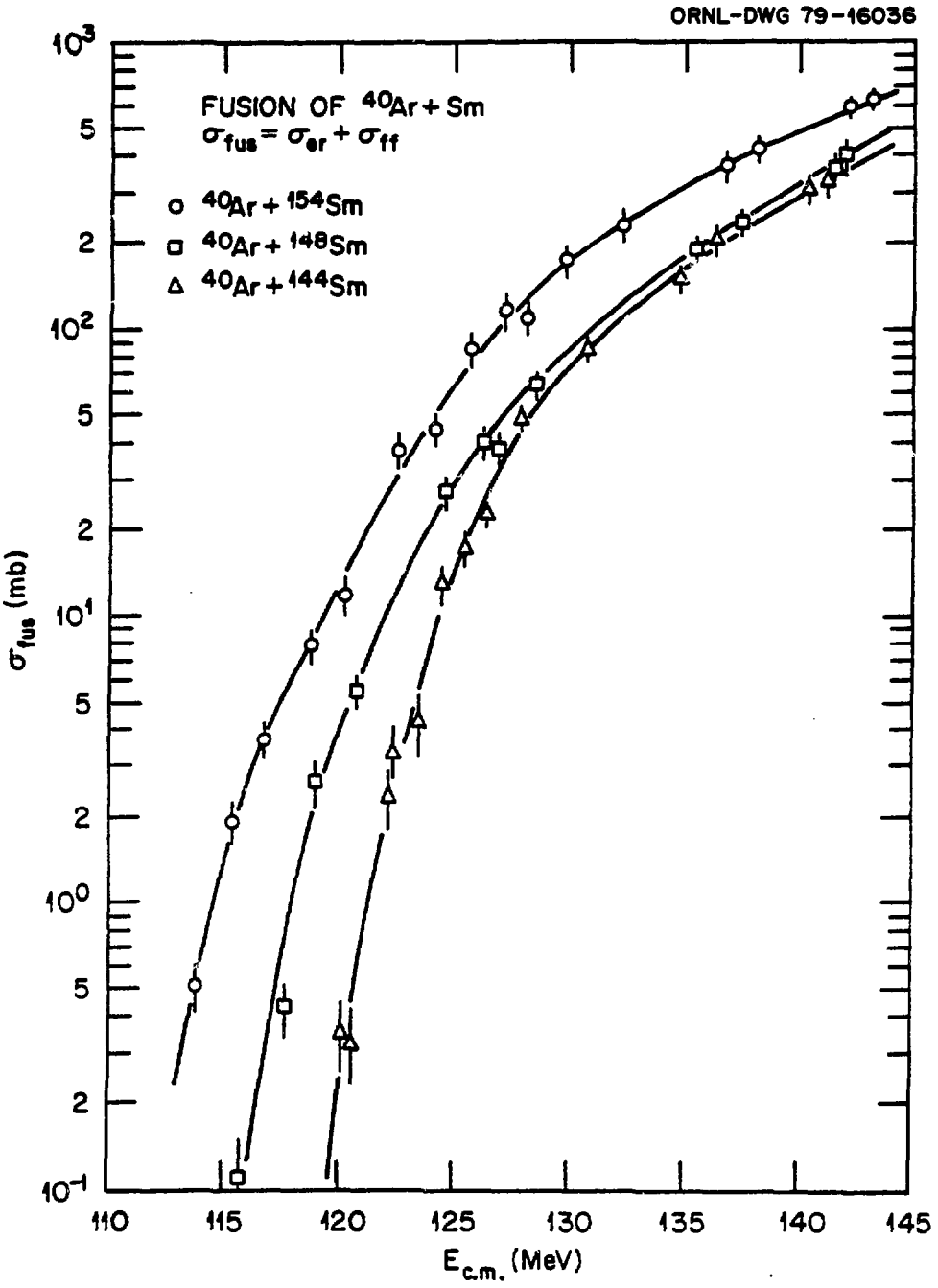
ORNL-DWG 79-16036
FUSION OF $^{40}Ar + Sm$
$\sigma_{fus} = \sigma_{er} + \sigma_{ff}$
$^{40}Ar + ^{154}Sm$
$^{40}Ar + ^{148}Sm$
$^{40}Ar + ^{144}Sm$
$\sigma_{fus}$ (mb)
$E_{c.m.}$ (MeV)

FIG. 9

ORNL-DWG 79-21215

ENERGIES AND COLLECTIVE STRENGTHS OF THE $2^+$ STATES OF Sm ISOTOPES

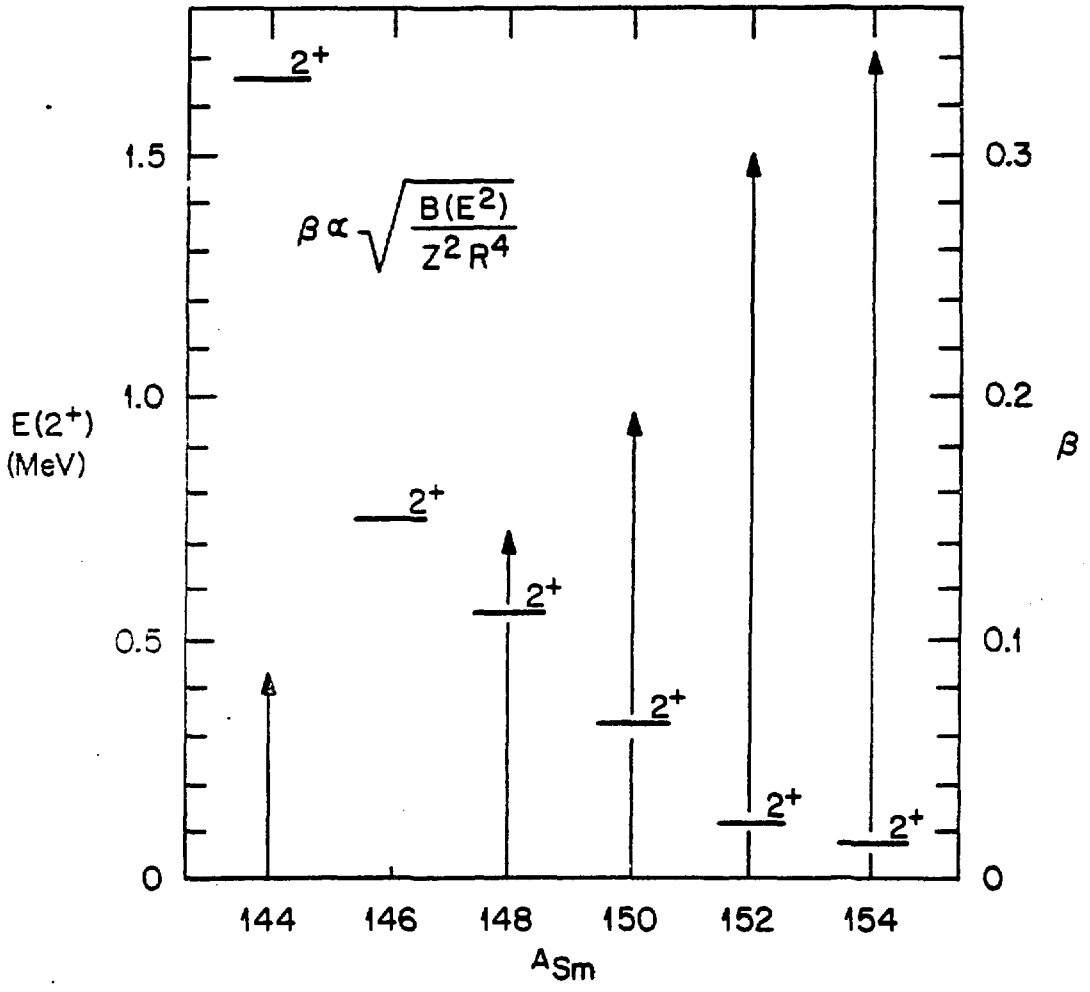


FIG. 10

ORNL-DWG 79-20754

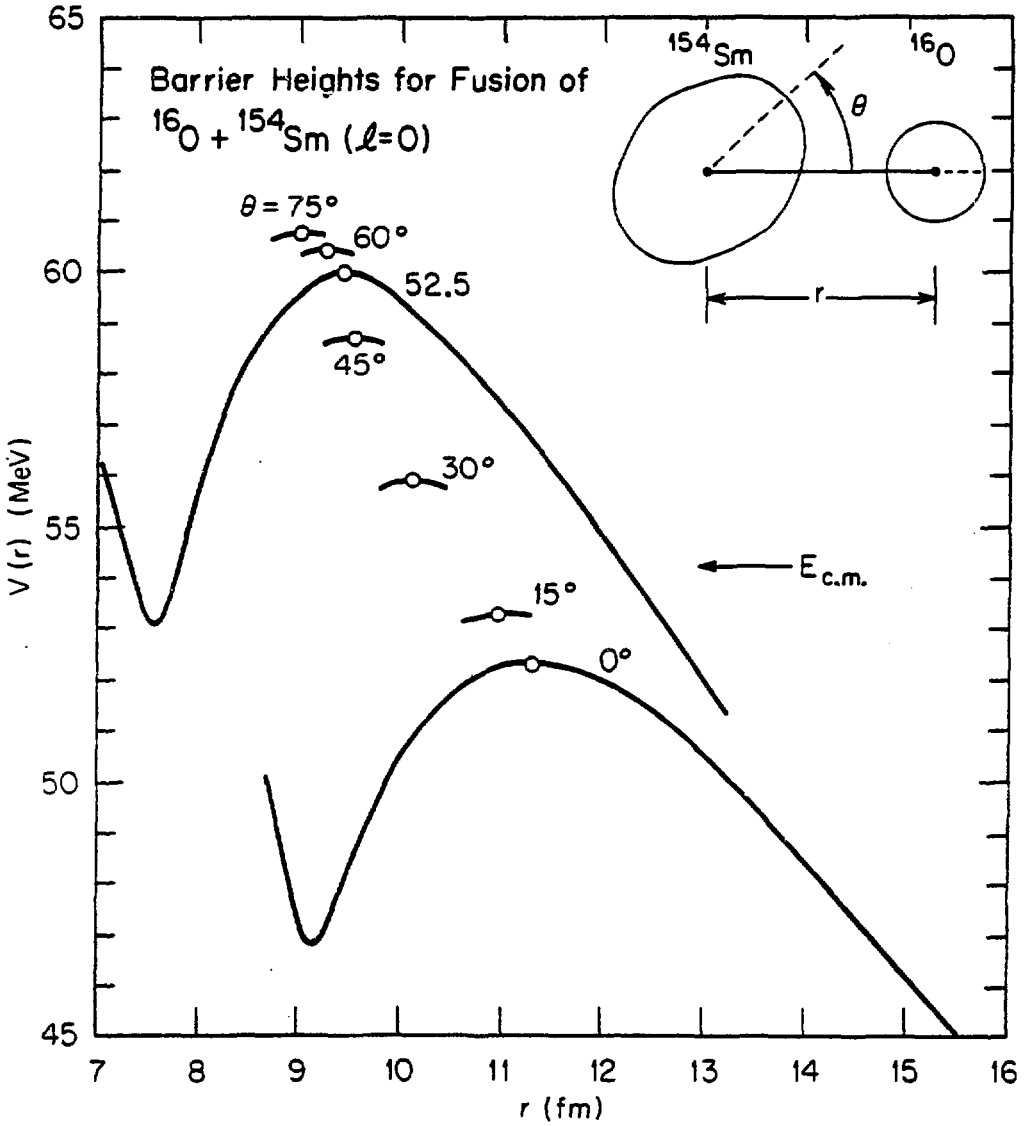


FIG. 11

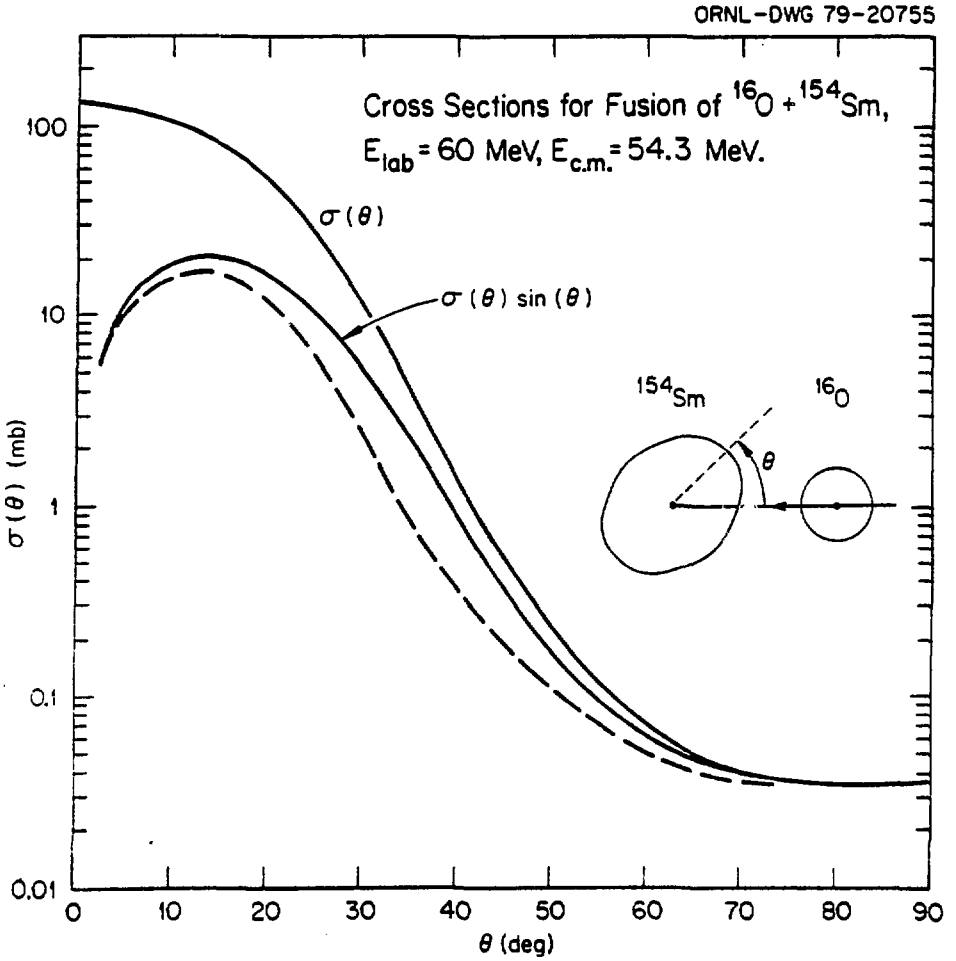
ORNL-DWG 79-20755
Cross Sections for Fusion of $^{16}O + ^{154}Sm$,
$E_{lab} = 60$ MeV, $E_{c.m.} = 54.3$ MeV.
$\sigma(\theta)$
$\sigma(\theta) \sin(\theta)$
$^{154}Sm$
$^{16}O$
$\theta$
$\sigma(\theta)$ (mb)
100
10
1
0.1
0.01
0
10
20
30
40
50
60
70
80
90
$\theta$ (deg)

FIG. 12

ORNL-DWG 79-20752

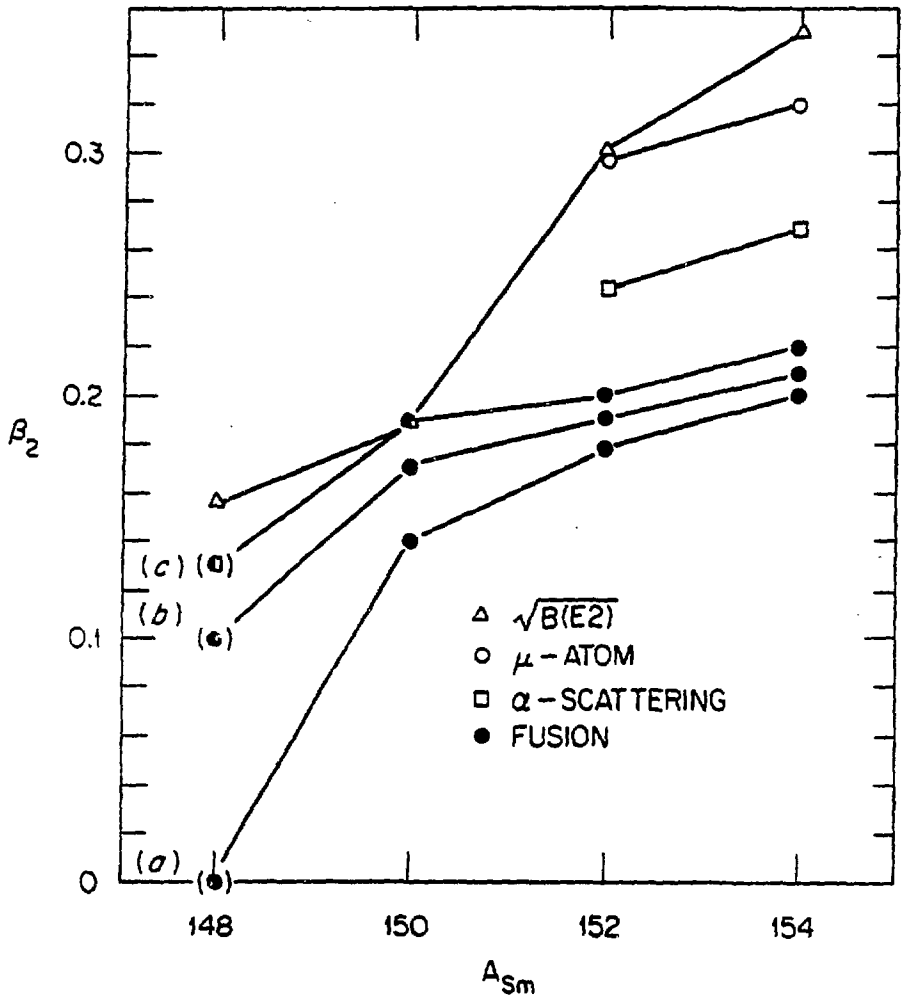


FIG. 13

ORNL-DWG 79-20750

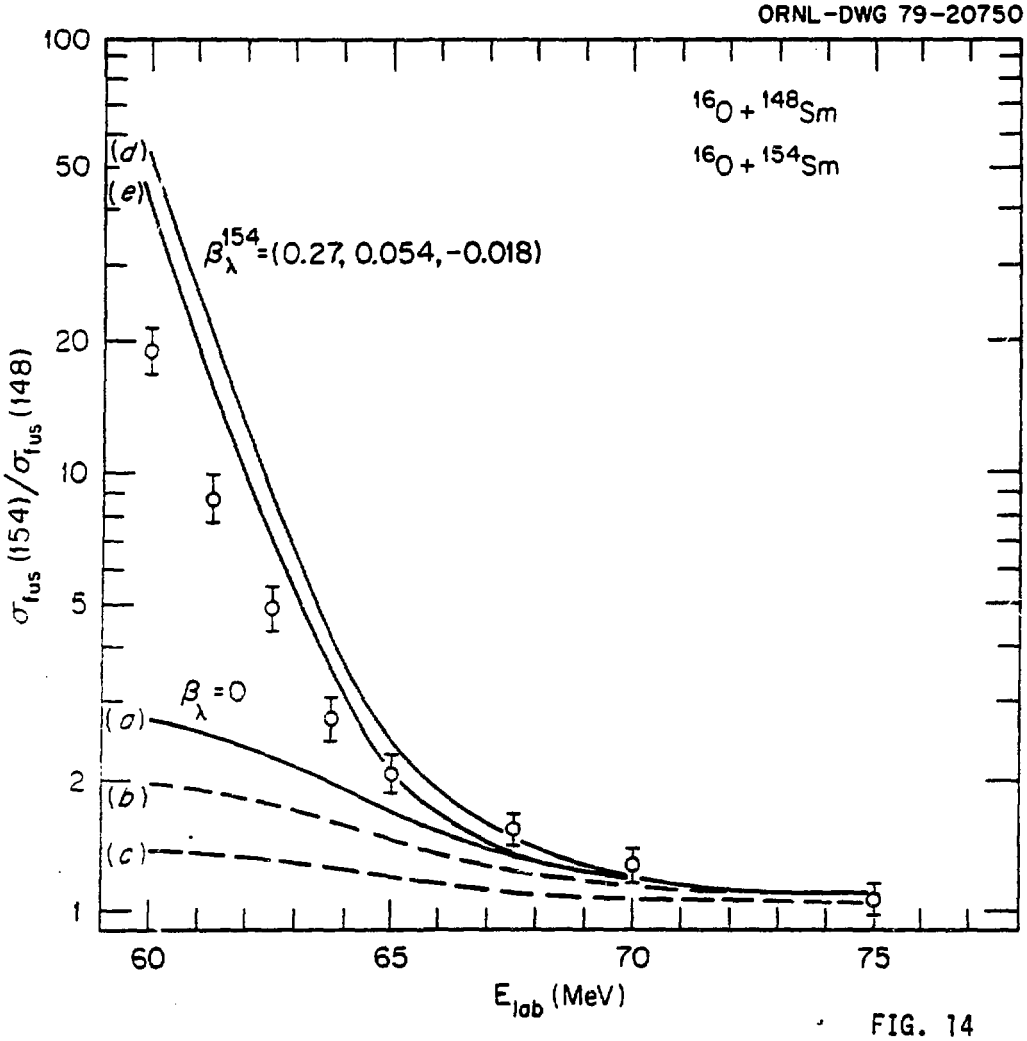


FIG. 14

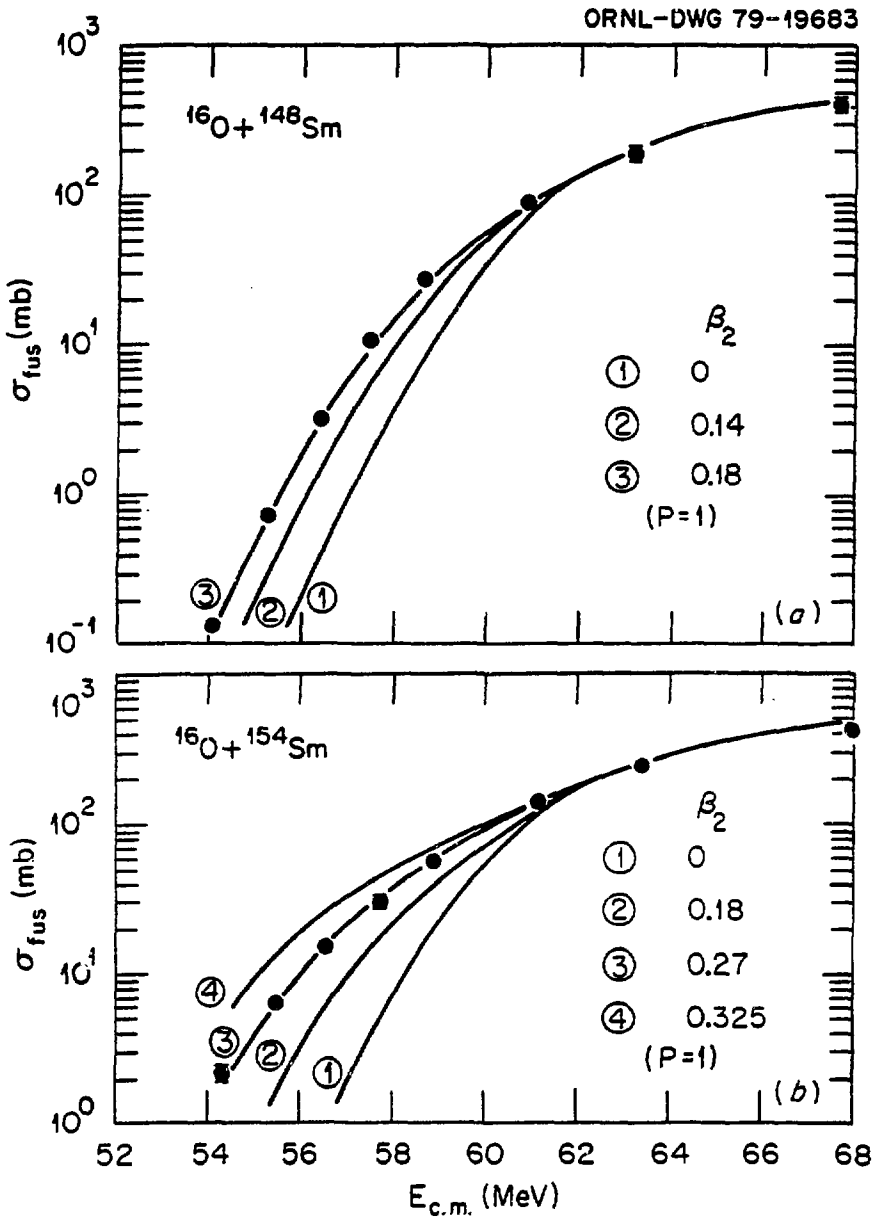
ORNL-DWG 79-19683
$^{16}O+^{148}Sm$
$\beta_2$
① 0
② 0.14
③ 0.18
(P=1)
(a)
$^{16}O+^{154}Sm$
$\beta_2$
① 0
② 0.18
③ 0.27
④ 0.325
(P=1)
(b)
$\sigma_{fus}$ (mb)
$E_{c.m.}$ (MeV)

FIG. 15

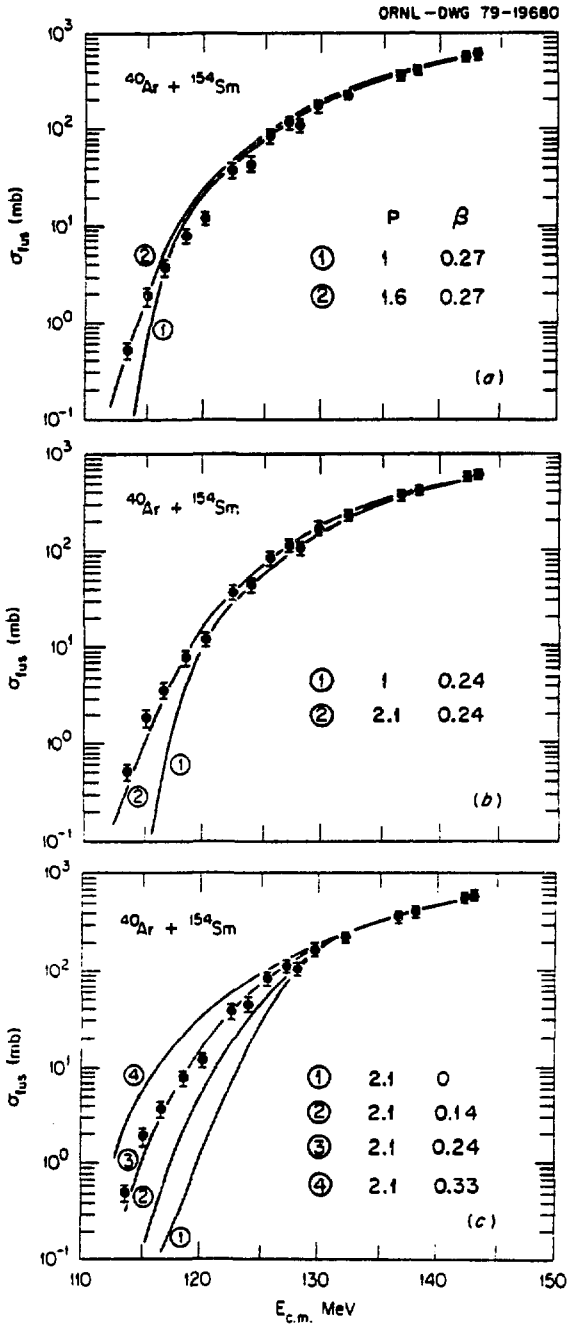
ORNL-DWG 79-19680
$^{40}$Ar + $^{154}$Sm
P β
① 1 0.27
② 1.6 0.27
(a)
$^{40}$Ar + $^{154}$Sm
① 1 0.24
② 2.1 0.24
(b)
$^{40}$Ar + $^{154}$Sm
① 2.1 0
② 2.1 0.14
③ 2.1 0.24
④ 2.1 0.33
(c)
$\sigma_{fus}$ (mb)
$E_{c.m.}$ MeV

FIG. 16

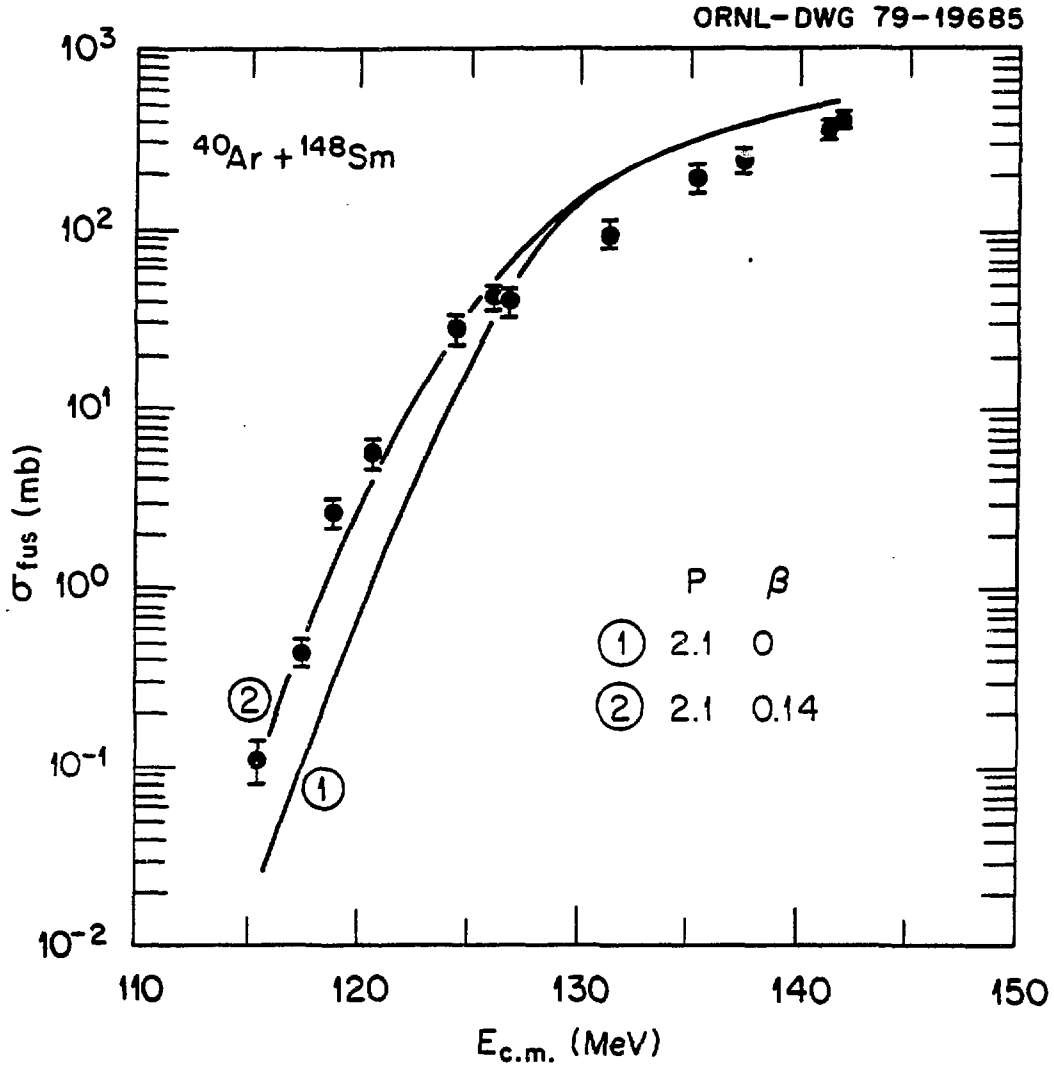
ORNL-DWG 79-19685
$^{40}Ar + ^{148}Sm$
$10^3$
$10^2$
$10^1$
$10^0$
$10^{-1}$
$10^{-2}$
$\sigma_{fus}$ (mb)
110
120
130
140
150
$E_{c.m.}$ (MeV)
P β
① 2.1 0
② 2.1 0.14
①
②

FIG. 17

ORNL-DWG 79-19686

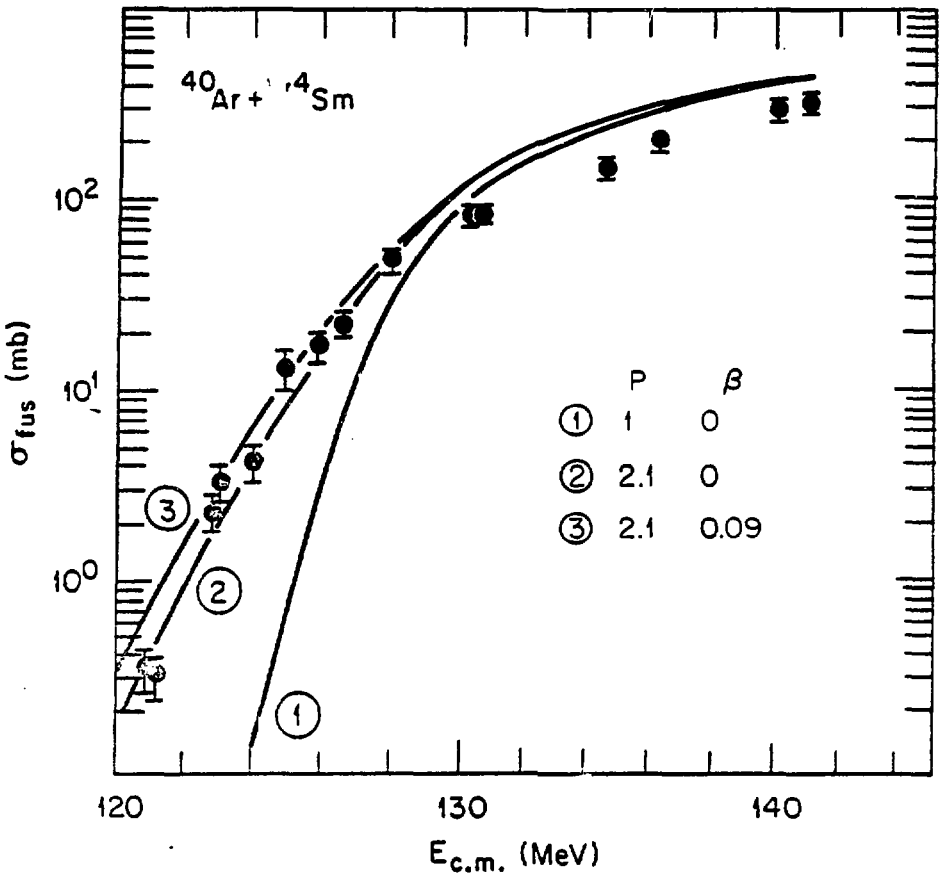


FIG. 18